PHYSICAL REVIEW D VOLUME 22, NUMBER 1 1 JULY 1980

Measurement and partial-wave analysis of the reaction $K^-p \rightarrow K_S^0\pi^+\pi^-n$ at 6 GeV/c

A. Etkin, K. J. Foley, J. H. Goldman,* R. S. Longacre, W. A. Love, T. W. Morris, S. Ozaki, E. D. Platner,
A. C. Saulys, C. D. Wheeler, and E. H. Willen
Brookhaven National Laboratory, Upton, New York 11973

S. J. Lindenbaum
Brookhaven National Laboratory, Upton, New York 11973
and City College of New York, New York, New York 10031

M. A. Kramer and U. Mallik
City College of New York, New York, New York 10031

(Received 5 February 1980)

We have performed a partial-wave analysis of the reaction $K^-p \rightarrow K_S^0\pi^+\pi^-n$ at 6 GeV/c. We present the results of the analysis of about 4500 events in the low-t region ($|t'| < 0.2$ GeV^2) for the dominant waves in the 1200-to-2000-MeV mass range. We observe the 2^+ $K^*(1430)$ and clear signals for the 1^+ $Q_2(1400)$ and the 3^- $K^*(1800)$. We find a new 1^- resonance at about 1500 MeV and have some evidence for another 1^- resonance at 1800 MeV. We also present the results of a partial-wave analysis as a function of t in the 1430-MeV mass region.

I. INTRODUCTION

We have studied the reaction

$$K^-p \rightarrow K_S^0\pi^+\pi^-n$$

at 6 GeV/c in a search for strange meson resonances in the $K\pi\pi$ system. The experiment was performed at the Brookhaven Alternating Gradient Synchrotron using the BNL multiparticle spectrometer. The charge-exchange channel was selected in order to avoid the large background problems in diffractive channels, primarily the Deck effect. We note that both natural- and unnatural-spin-parity resonances can decay via the $K\pi\pi$ mode.

The present state of K^* spectroscopy is quite complex due to the large number of wide overlapping resonances. To resolve these states, a partial-wave analysis is necessary. The high-statistics partial-wave analyses have been mostly performed on the diffractive channels which suffer from large backgrounds.[1] We have performed a partial-wave analysis of ~4500 events at low t' in the charge-exchange channel in the $K\pi\pi$ mass range from 1200 to 2000 MeV.

Section II describes the experiment and the data analysis. Section III summarizes the cuts which have been applied to the recorded event candidates. The results are presented in Secs. IV and V, and compared with two other partial-wave analyses for this reaction.[2,3] In Sec. VI, we attempt to relate the K^* states found in this analysis to the simple quark model. The results of a partial-wave analysis as a function of t in the 1430-MeV mass region and the production cross section of the 2^+ K^* (1430) state is given in Sec. VII.

II. APPARATUS AND EXPERIMENTAL PROCEDURE

This experiment used the BNL multiparticle spectrometer (MPS) in the medium-energy separated beam (MESB) of the Alternating Gradient Synchrotron (AGS).

A. Experimental setup

At 6 GeV/c the electrostatically separated MESB provided a K^- flux of approximately 10 000 per pulse with a K/π ratio of $\frac{1}{4}$. Two threshold Čerenkov counters were used to identify kaons, reducing the net pion contamination to less than 1%. The $\bar{p}$ contamination was negligible. The beam spectrometer, consisting of an 8° bending magnet and six sets of proportional wire-chamber planes (PWC's), measured the incident angle to ±1 mrad (rms) and the momentum to ±0.4% (rms).

The reaction products were detected using the MPS, which is shown in Fig. 1. The magnet is a large C magnet with pole dimensions of 457 cm × 183 cm and a gap height of 122 cm; the central field was 10 kG. A 7.6-cm-diameter, 51-cm-long liquid-hydrogen target was located near the upstream end of the MPS. The main detectors were 14 modules of spark-chamber planes with magnetostrictive readout arranged approximately per-

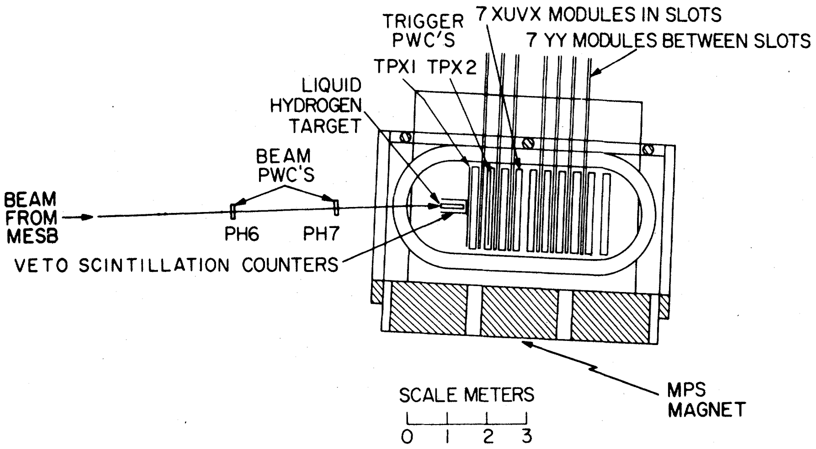

FIG. 1. Layout of the MPS for this measurement.

pendicular to the beam direction. As shown in Fig. 1, *XUVX* modules (two gaps with vertical wires and one each at ±15° to the vertical) alternated with *YY* modules (two gaps with horizontal wires). In any gap the wires were parallel, with both sides read out, each readout encoding up to eight sparks. The active area of the spark chambers was 170 cm×110 cm. The angular and momentum resolution of the spectrometer for 6-GeV/*c* tracks were ~1 mrad and ~1%, respectively, attributable largely to multiple scattering.

The trigger was accomplished with the aid of two PWC's—*TPX*1 (120 cm ×105 cm, 2.5-mm wire spacing), located just downstream of the H_2 target, and *TPX*2 (170 cm×105 cm, 2.5-mm wire spacing), located 56 cm downstream from *TPX*1. *TPX*1 was electronically divided into three sections, *TPX*1*L*, *TPX*1*C*, and *TPX*1*R*. An open-ended scintillation-counter veto box (38 cm×38 cm ×96 cm long) surrounded the target. For part of the experiment the veto box was lined with 3-mm-thick lead sheets to provide a γ-ray veto. A more detailed description of the apparatus is given in Ref. 4.

B. Trigger selection

The topology of the events of interest consisted of a production vertex in the target with two outgoing charged pions and a neutral kaon which decayed into two charged pions downstream. Good coverage of phase space required accepting events where the K^0 decay occurred anywhere between the production vertex and the second trigger detector *TPX*2. Thus, either two or four charged pions might be detected in the first trigger plane *TPX*1. For almost all of the desired events all charged particles passed through the central 40 cm of *TPX*1, the section called *TPX*1*C*. *TPX*1*L* and *TPX*1*R* were thus used as a veto in the trigger to help suppress triggers from interactions upstream of the H_2 target. Studies showed that the trigger rate was not too dependent on the maximum number of hits allowed in *TPX*2, so in order to reduce event losses due to noise, etc., the trigger permitted four to six hits in *TPX*2. Since the events of interest had neutron recoils, the veto box was used in anticoincidence. Thus, the final trigger was

$$(\text{Incident kaon})\cdot TPX1C\ (2,\ 3,\ \text{or}\ 4\ \text{hits})\cdot TPX2\ (4, 5,\ \text{or}\ 6\ \text{hits})\cdot \overline{(\text{target veto box})}\cdot \overline{TPX1L}\cdot \overline{TPX1R}\ .$$

The trigger rate was 1 per 1000 incident kaons or about 10 per AGS pulse. We recorded one additional trigger for each AGS pulse with no restriction other than requiring an incident-beam kaon ("profile" trigger) which was used to monitor the performance of the spark chambers and PWC's.

C. Experimental procedure

Data were recorded for 250 hours in two approximately equal running periods. Information from all detectors was encoded, formatted, and written into the buffer memory of a data handler (DH) during the AGS spill. The capacity of the DH was sufficient to store the data from all triggers which could be generated during one spill. Between spills the data were written on magnetic tape and simultaneously a sample of the events was transferred to the DEC KA10 computer of the BNL on-line data facility. In addition to the detector data, information from a rapid-cycling digital voltmeter (DVM) and a set of CAMAC scalers were recorded.

The DVM was used to monitor the readings of Hall probes and current shunts for all of the magnets in the experiment, as well as power-supply voltages, temperatures, etc. The beam rate and trigger rates were monitored continuously to ensure stable operation of the experiment.

Periodically we recorded data from profile triggers with the magnetic field turned off. These data tapes were used to determine the precise origins of the spark-chamber coordinates relative to the incident-beam detectors.

The program running in the on-line computer did complete reconstruction of a sample of the events as well as checking the format of the data, the performance of the detectors, and the stability of the DVM readings. The event reconstruction included pattern recognition to find tracks and vertices, geometrical fits to the track angles and momenta, and calculation of kinematic quantities such as the $\pi^+\pi^-$ effective mass and the missing mass from four-prong events. Spark-chamber efficiencies were calculated from the "profile" event sample on the basis of whether the chamber had a spark corresponding to the fitted beam track. The KA10 ran in a real-time mode so that warning messages could be typed immediately after a malfunction was detected. Cathode-ray tube displays of events, pattern recognition performance, and histograms of apparatus performance and kinematic quantities could be viewed during data recording.

D. Event reconstruction

The approximately 400 magnetic tapes of data were processed on the CDC 7600 computer of the BNL central scientific computing facility (CSCF). The primary processing program did full event reconstruction and a coarse event selection for further analysis. The reconstruction results of each accepted event were written as a single record on the data-summary tapes.

1. Data unpacking and corrections

The coordinates of the hits in each detector were reconstructed from the encoded data record and corrections were applied for thermal effects and the "$E\times B$ effect," i.e., the displacement of the detected position due to the effect of the magnetic field on the moving electrons as they are accelerated by the electric field in the spark chamber. The displacement of sparks in "profile" events from the projected beam track was used to evaluate the magnitude (~1 mm) of this correction.

2. Pattern recognition and geometry

Over the volume occupied by the spark chambers the magnetic field of the MPS is nearly vertical (parallel to y axis) and thus tracks are helices about the y axis. Detectable tracks are produced in the generally forward direction and have momenta greater than 200 MeV/c. The initial segment of the yz projection of these tracks is almost straight. Track pattern recognition thus started by searching for straight-line correlations of sparks in the YY modules. Each straight-line segment so found was used to compute the x coordinate corresponding to each U and V readout in an $XUVX$ module.

The resulting four arrays of x coordinates (two true x and two projected uv) were then scanned for combinations that were spatially correlated. The x combinations which best formed an apparent track element were associated with the y track, and the assembly of these elements in the several $XUVX$ modules was checked for an approximate fit to a circle in the xz plane. A three-dimensional helix was then used to search for any further sparks associated with this track and to combine track fragments. The actual algorithm was, of course, much more complicated and involved many strategems to handle special cases.

A least-squares fit based on the method of TVGP (Ref. 5) was used to calculate the value of the track parameters, namely, the azimuth, the dip (pitch) of the helix, the momentum, and the coordinates of a point at the upstream end of the track. For this purpose, an accurate representation of the MPS magnetic field was used.

After the tracks were fitted, a search for vertices was performed. A decay vertex was defined as the weighted mean of the points of closest approach of the two oppositely charged particle tracks which appeared to intersect within the decay fiducial volume, the region from the upstream end of the H_2 target to the location of $TPX2$. The effective mass at each decay vertex was calculated for three hypotheses: K_S^0, Λ, and $\overline{\Lambda}$. If the effective mass of the neutral vee for any of the above three cases was within an acceptable mass range (475–525 MeV for K_S^0, 1100–1130 MeV for Λ and $\overline{\Lambda}$), the vertex was tagged accordingly.

Subsequently, a search was made for production vertices. A production vertex was defined by the simultaneous intersection within the target of two outgoing tracks and a beam track. The two tracks tagged previously as forming a K_S^0 decay vertex were excluded from the production-vertex search. This caused a depletion of events whose production vertices had a $\pi^+\pi^-$ effective mass near the K^0 mass. In order to represent the depletion cleanly, events in this region were removed by a cut described in Sec. III (cut 8), which was also applied in all acceptance calculations and Monte Carlo data simulations. Events with a K_S^0 decay vertex and a two-prong production vertex with a missing mass squared (MM^2) from the $K^0\pi\pi$ system in the range $0.36 < \text{MM}^2 < 1.44$ GeV^2 were selected. The K_S^0 mass band and this MM^2 band were wide enough to include substantially all the actual events of the desired reaction and enough of the tails of the distributions to make meaningful estimates of background possible after further analysis. Track and vertex information from approximately 70 000 such event candidates were written on data-summary tapes for further analysis.

3. Constrained fit

The events were fitted using the applicable geometric and kinematic constraints. The incident-beam track, the reconstucted K_S^0, and the two charged pions were constrained to intersect at a single point in space. The K_S^0 effective mass and the $K_S^0\pi^+\pi^-$ missing mass (neutron) were fixed at the conventional values.

III. CUTS

A. $K_S^0\pi^+\pi^-n$ event selection

The cuts applied to the events on the data summary tapes and the fraction of events failing each cut are listed in Table I. The explanation of each cut follows.

Cut 1. The short-track cut was imposed since the apparatus acceptance and the reconstruction efficiency of the pattern recognition program was extremely difficult to evaluate for events containing short tracks. An event was discarded unless all four tracks reached the last gap of the second *XUVX* module, ~120 cm from the center of the H_2 target.

TABLE I. Cuts applied to the reconstructed events and the effect of each at two levels. The cuts are defined in Sec. III. Condition 1: fraction of event candidates removed by each cut individually when all cuts 1 through 7 are imposed. Condition 2: same as condition 1, with additional imposition of cuts 9 and 10 (see text).

No.	Cut	Fractional event losses Condition 1	 Condition 2
1	Short track	14%	12%
2	K_S-Λ overlap	0.3%	0.2%
3	$K_S\pi^-p$	12%	3%
4	$\Delta z/\delta z$	13%	13%
5	Constrained fit	2%	2%
6	K_S^0 eff. mass	23%	23%
7	$K_S\pi^+\pi^-(\text{MM})^2$	32%	27%
	Events remaining	13 532	4985

Cut 2. K_S^0-Λ overlap: The decay products from the neutral vee were not identified. Hence, to ensure a clean K_S^0 sample, an event was rejected if the effective mass of the neutral vee under the Λ or $\bar{\Lambda}$ hypothesis was in the range 1110 to 1120 MeV.

Cut 3. There is a contamination of events from the reactions

$$K^-p \to K_S^0\pi^-p$$

and

$$K^-p \to K_S^0\pi^-p\pi^0 ,$$

where the proton is misinterpreted as a π^+. We have calculated the missing mass squared for the $K_S^0\pi^-p$ hypothesis and see a narrow peak at low missing mass squared. We have removed all events for which

$$-0.01 < \text{MM}^2(K_S^0\pi^-p) < 0.09 \text{ GeV}^2.$$

Cut 4. Four-prong production vertex: Events with $\Delta z/\delta z < 2.0$ were eliminated, where Δz is the distance between the production and decay vertices and δz is the standard deviation on Δz. This was done to eliminate events of the reactions

$$K^-p \to K^-\pi^+\pi^-p$$
$$\to K^-\pi^+\pi^-\pi^+n$$

from the data sample.

Cut 5. Constrained-fit cut: Events for which the constrained fit failed to converge or for which the χ^2 of the fit was worse than 1.4 times the number of degrees of freedom were removed.

The yield after all five of these cuts had been applied was 26 491 events.

Cut 6. The final K_S^0 mass selection removed all events for which the effective $\pi^+\pi^-$ mass for the decay vertex was outside the range 489 to 503 MeV.

Cut 7. Neutron recoils were selected by requiring the square of the missing mass from the $K_S^0\pi^+\pi^-$ system to be inside the range 0.75 to 1.05 GeV^2.

Cuts 6 and 7 correspond to approximately 2-standard-deviation regions (our resolution is not quite Gaussian) on either side of each peak. The loss of events due to the tails of the K^0 and MM^2 peaks was accounted for in the calculations of the total cross section for $K^*(1430)$ production (Sec. VII). Figure 2 shows the decay-vertex $\pi^+\pi^-$ effective-mass distribution for the data, with all the above cuts applied except cut 6. The K_S^0 peak

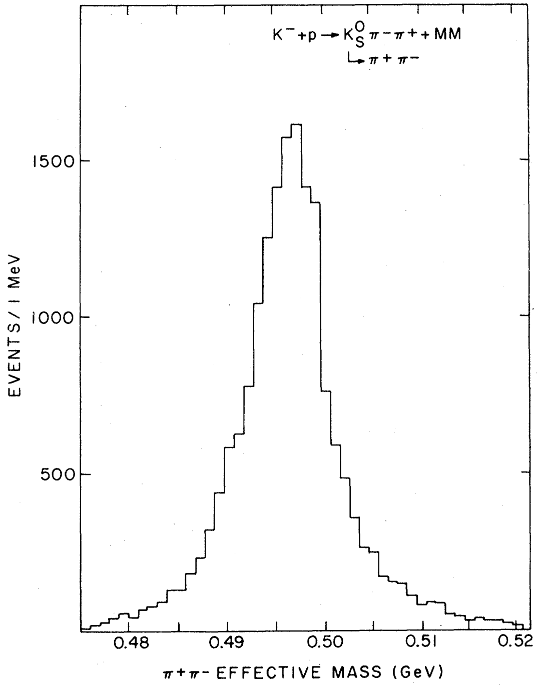

FIG. 2. Spectrum of the $\pi^+\pi^-$ effective mass for the decay vertex. Cuts 1–5 and cut 7 have been applied (see Sec. III).

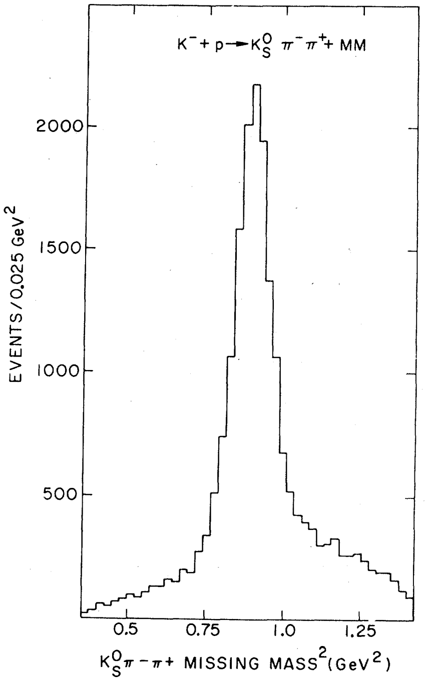

FIG. 3. Spectrum of the square of the missing mass from the $K^0_S\pi^+\pi^-$ system. Cuts 1–6 have been applied.

is centered at 497.0 MeV. The discrepancy from the accepted K^0_S mass (497.7 MeV) is due chiefly to systematic errors in the determination of the opening angle between the decay pions. Plotted in Fig. 3 is the $K^0_S\pi^+\pi^-$ missing-mass-squared distribution after cuts 1 through 6. The neutron peak is centered at 0.91 GeV^2. The discrepancy from the expected MM^2 value (0.88 GeV^2) is due chiefly to uncertainty in the calibration of the magnets of the incident-beam spectrometer. The background remaining after these cuts is estimated to be about 15%. The net yield after cuts 1–7 was 13 532 events, for which the $K^0_S\pi^+\pi^-$ mass spectrum is shown in Fig. 4. The mass values were calculated from the measured track parameters before the constrained fit. Figure 5 shows the $K^0_S\pi^-$ effective-mass spectrum for the same event sample. A $K^*(890)^-$ peak dominates the spectrum. Figures 6 and 7 show the effective-mass spectra of $K^0_S\pi^-$ and the $K^0_S\pi^+\pi^-$ from the kinematically constrained (fitted) data. The spectra before and after the kinematic constraint (Fig. 5 compared with Fig. 6 and Fig. 4 compared with the open histogram in Fig. 7) were basically the same. The bump in the $K^0_S\pi^+\pi^-$ mass spectrum at 1430 MeV corresponds to ~200 events/μb after corrections for the acceptance (obtained using

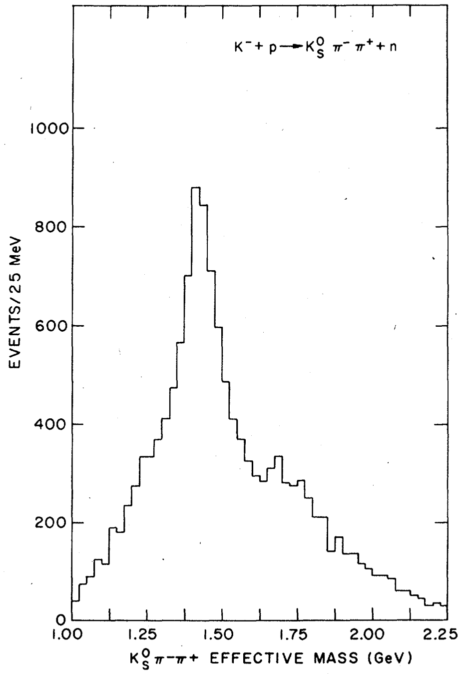

FIG. 4. $K^0\pi^+\pi^-$ effective-mass spectrum after cuts 1–7, calculated without kinematic constraints.

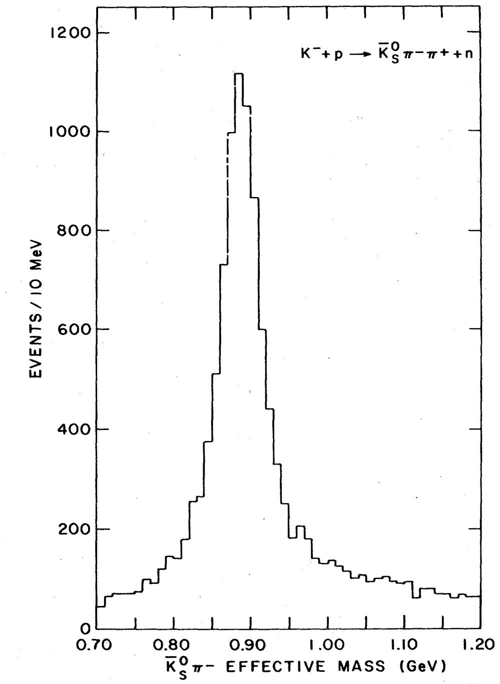

FIG. 5. $K^0_S\pi^-$ effective-mass spectrum for the events of Fig. 4 (unconstrained).

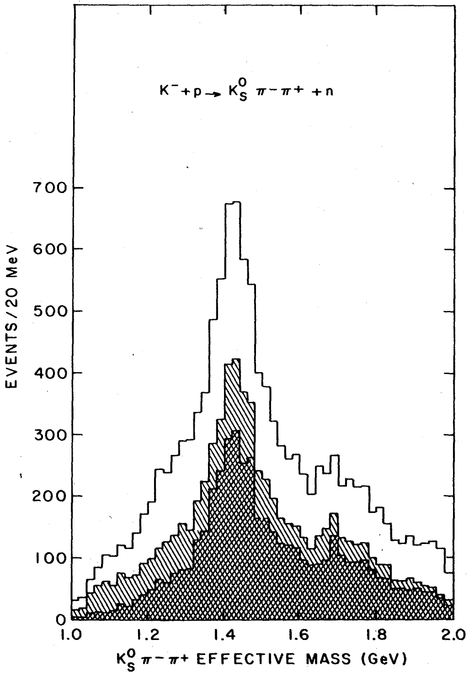

FIG. 7. $K^0_S\pi^+\pi^-$ effective-mass spectrum, constrained fit. Open histogram: events after cuts 1–7. Singly cross-hatched histogram: events with $|t'_{K\pi\pi}| < 0.2$ GeV^2. Doubly cross-hatched histogram: N^* removed.

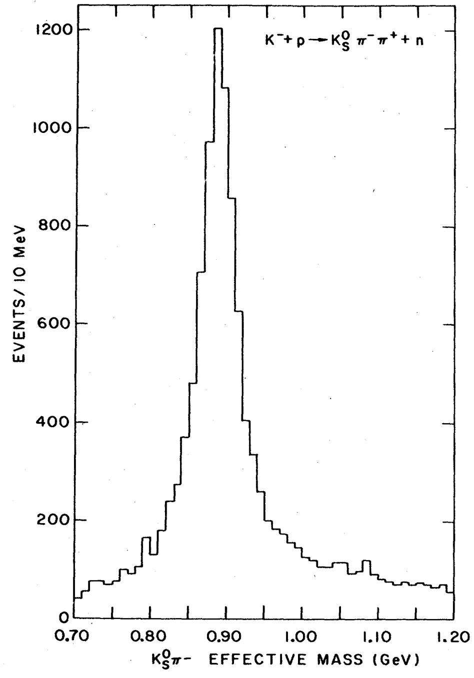

FIG. 6. $K^0_S\pi^-$ effective-mass spectrum calculated using kinematic constraints.

phase-space distributions) and for cuts 1 through 7. The kinematically constrained data was used for further analysis.

In an earlier publication[6] we presented ~9500 events from the first analysis of this experiment showing a narrow peak in the $K^0_S\pi^+\pi^-$ mass spectrum at ~1.7 GeV. The more complete analysis reported here has yielded ~13 500 events. As can be seen from Fig. 7, a bump still appears at ~1.7 GeV, but the effect is now too small for any claim. A definitive statement on narrow structure in this region must await partial-wave analysis of high-statistics experiments; as will be seen later, the present data sample does not permit partial-wave analysis in very narrow mass bins.

B. Selection of the sample for partial-wave analysis

Cut 8. As stated in Sec. II D 2, the vertex-search procedure causes a depletion of events with $\pi^+\pi^-$ (production vertex) effective mass in the region of the K^0_S mass. To make this loss well-defined and reproducible in the Monte Carlo event generation we have removed all events with production-vertex pion-pair effective mass in the range 475 to 525 MeV. This cut removed an additional 682 events.

Cut 9. t' selection: For the $K_S^0\pi^+\pi^-$ mass-scan partial-wave analysis, we selected events with $|t'| < 0.2$ GeV^2 in order to select primarily events produced by pion exchange; t' is defined as $t - t_{\min}$, where t is the four-momentum transfer squared to the $K\pi\pi$ system. The $K_S^0\pi^+\pi^-$ mass spectrum of the small-t' events is shown as the single cross-hatched histogram in Fig. 7. There were 7306 events included in this region.

Cut 10. N^* cut: The purpose of the partial-wave analysis was to search for resonances which decay into $K\pi\pi$. However, there is a kinematic overlap of the reaction $K^-p \to K^*N^*$ with the reaction $K^-p \to (K\pi\pi)n$. The dominant N^* cross section is $K^-p \to K^*(890)N^*$ produced by π exchange (see Fig. 8). We also observe N^* production along with other $K\pi$ isobars, the κ and the $K^*(1420)$. Since N^* production is associated with π exchange, the N^*'s are produced predominantly with low momentum transfer to the $K\pi$ subsystem. In order to reduce the N^* background, we have removed all events with $|t'_{K\pi}| < 0.25$ GeV^2 and $M(n\pi^+) < 1800$ MeV. We have found that at low $|t_{K\pi\pi}|$, $t_{K\pi}$ and $t_{K\pi\pi}$ are approximately independent variables. This makes it practical to remove most N^*'s from this $t_{K\pi\pi}$ region by this simple $t'_{K\pi}$ cut. This cut left 4985 events in the selected $t'_{K\pi\pi}$ region, which are shown as the doubly cross-hatched histogram on Fig. 7.

IV. PARTIAL-WAVE ANALYSIS

The partial-wave analysis (PWA) was performed using the Berkeley-SLAC program[7] adapted to $K_S^0\pi^+\pi^-$. The PWA was carried out initially in the $K\pi\pi$ mass region 1200 to 1600 MeV. After some necessary physics assumptions we were able to propagate our solution to 2000 MeV.

A. The model

In order to proceed with the presentation of the partial-wave analysis, we need to review briefly the isobar model,[7] and discuss the labeling of the resulting partial-wave amplitudes. The isobar model describes the three-body final state as a superposition of two-body states, each involving an isobar and a "bachelor" particle. The isobars used for this analysis are the $K^*(890)$ and ρ vector-meson states and the K-π s-wave scattering state represented as κ. The amplitude is then defined in terms of $J^P(\text{isobar})LM^\eta$, where J is the spin, P is the parity, (isobar) is the isobar state being considered (K^*, ρ, κ), L is the relative orbital angular momentum between the isobar and the bachelor particle (see Fig. 9) M is the magnetic substate, and η is the naturality of the exchange in the t channel [defined as $\eta = (-1)^{J'} \times P'$, where J' and P' are the spin and parity of the exchange particle]. Since the incident K^- are pseudoscalars, η for the $M = 0$ level is given by $\eta = (-1)^J \times P$, where J and P refer to the spin and parity of the produced state. For example, the $M = 0$ level of the well-known tensor $K^*(1430)$ would appear in the amplitude labeled $2^+K^*D0^-$, while the Q_2 meson would appear in the amplitude labeled $1^+K^*S0^+$. These isobar amplitudes depend upon seven variables: s, t, $s_{K\pi}$, $s_{\pi\pi}$, α, β, γ, where s is the mass squared of the $K\pi\pi$ system, t is the momentum transfer squared to the $K\pi\pi$ system, $s_{K\pi}$ is the mass squared of the $K^0\pi^-$ subsystem, $s_{\pi\pi}$ is the mass squared of the $\pi\pi$ subsystem, and α, β, γ are the three Euler angles which rotate from the Gottfried-Jackson system to the Dalitz system; α is the azimuthal angle around the bachelor-particle direction, β is the Jackson angle between the beam-particle and the bachelor-particle direc-

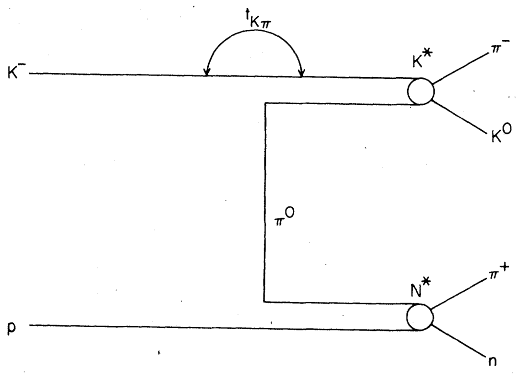

FIG. 8. π-exchange diagram for the reaction $K^-p \to K^*N^*$.

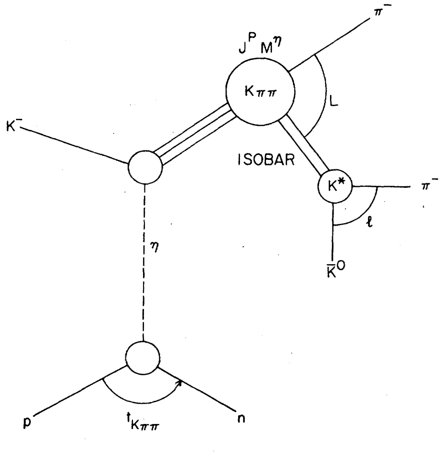

FIG. 9. Schematic diagram describing the isobar model for $K^-p \to K_S^0\pi^+\pi^-n$ scattering. The variables are described in the text.

tions, and γ is the azimuthal angle around the beam-particle direction. In this analysis, the Gottfried-Jackson system is defined so that the K^- beam direction is the z axis, and the y direction is $\vec{p}_p \times \vec{p}_n$.

B. Binning of the data for partial-wave analysis

The above seven variables can be reduced to five by binning in s and cutting on t. The binning of s, of course, is done in the mass of the $K_S^0\pi^+\pi^-$ system which is the square root of s. Bins in mass were selected from 60 to 100 MeV in width, depending on the available statistics. The bins and the number of events used in the analysis are shown in Table II. For the t cut (cut 9) we used $|t'| < 20\ \mathrm{GeV}^2$.

TABLE II. Mass bins used for the low-t partial-wave analysis and the number of events in each bin.

Bin central value (MeV)	Width (MeV)	No. of events
1240	80	246
1310	60	290
1370	60	594
1430	60	853
1490	60	587
1560	80	500
1650	100	507
1750	100	465
1850	100	281
1950	100	196
Total		4519

C. Acceptance calculation

A Monte Carlo program was used to calculate the acceptance of the apparatus. From 5×10^4 to 2×10^5 events per mass bin were generated according to a three-body phase space, with $d\sigma/dt \propto e^{4t}$. The experimental conditions such as the magnetic field, the detector locations, and the trigger criteria were simulated in the program. Appropriate cuts were applied to the Monte Carlo events to simulate the effect of the cuts applied to the real data. In order to perform a partial-wave analysis the acceptance was calculated for each partial wave individually. A full acceptance matrix was developed, including the acceptance for each wave and for the effect of interference between waves. The acceptances for the important waves in the 1430-MeV bin are given in Table III.

D. Initialization of partial-wave analysis and selection of solutions in the 1200-1600 MeV region

The partial-wave-analysis (PWA) program uses the fitting program OPTINE.[8] OPTINE uses the maximum-likelihood method in order to adjust the production amplitudes to best describe the experimental data, and obtains errors on the production amplitudes by calculating the inverse of the second derivative matrix at the solution.

The first step in our PWA fitting involved a series of random searches with ~50 different sets of waves in the 60-MeV bin centered at 1430 MeV. This bin was chosen because it represents the largest available statistics. All waves up to $J=2$ for $M=0$ or 1 were tried in various combinations. For each wave set, typically 100 random starting points were tried, and the five with the highest likelihood were propagated through 20 optimizing steps searching for the best fit. Waves were eliminated from searches if their amplitudes were small compared to their errors.

Approximately ten solutions obtained from these random searches were propagated up and down in mass in order to obtain a continuous solution. If a solution showed discontinuities in only one or two waves, it was tried again without these troublesome waves. This procedure yielded one preferred solution in the region 1200–1600 MeV on the grounds of likelihood. The logarithmic likelihood of the nearest different solution was lower by 25. Scaling from a Monte Carlo study[9] of the relative error in logarithmic likelihood between different partial-wave solutions to the same set of data, we estimate that this corresponds to a 4-standard-deviation worse fit. We tried to find additional solutions by doing random searches at the lowest-mass bin and propagating them up in mass. However, no new solution was found which was competitive in likelihood.

E. Comparison of fit with the data

In order to examine the quality of our fit, we made a comparison with the data at the 1430-MeV bin. We took our solution at this mass and generated a Monte Carlo set of events using the finally

TABLE III. Acceptance of the apparatus for six partial waves in the mass bin from 1400 to 1460 MeV.

Wave $J^P(\text{isobar})LM^\eta$	Acceptance (%)
$1^+K^*S0^+$	12
$0^-\kappa S0^+$	15
$1^-K^*P0^-$	21
$1^-\rho P0^-$	28
$2^+K^*D0^-$	13
$2^+\rho D0^-$	20

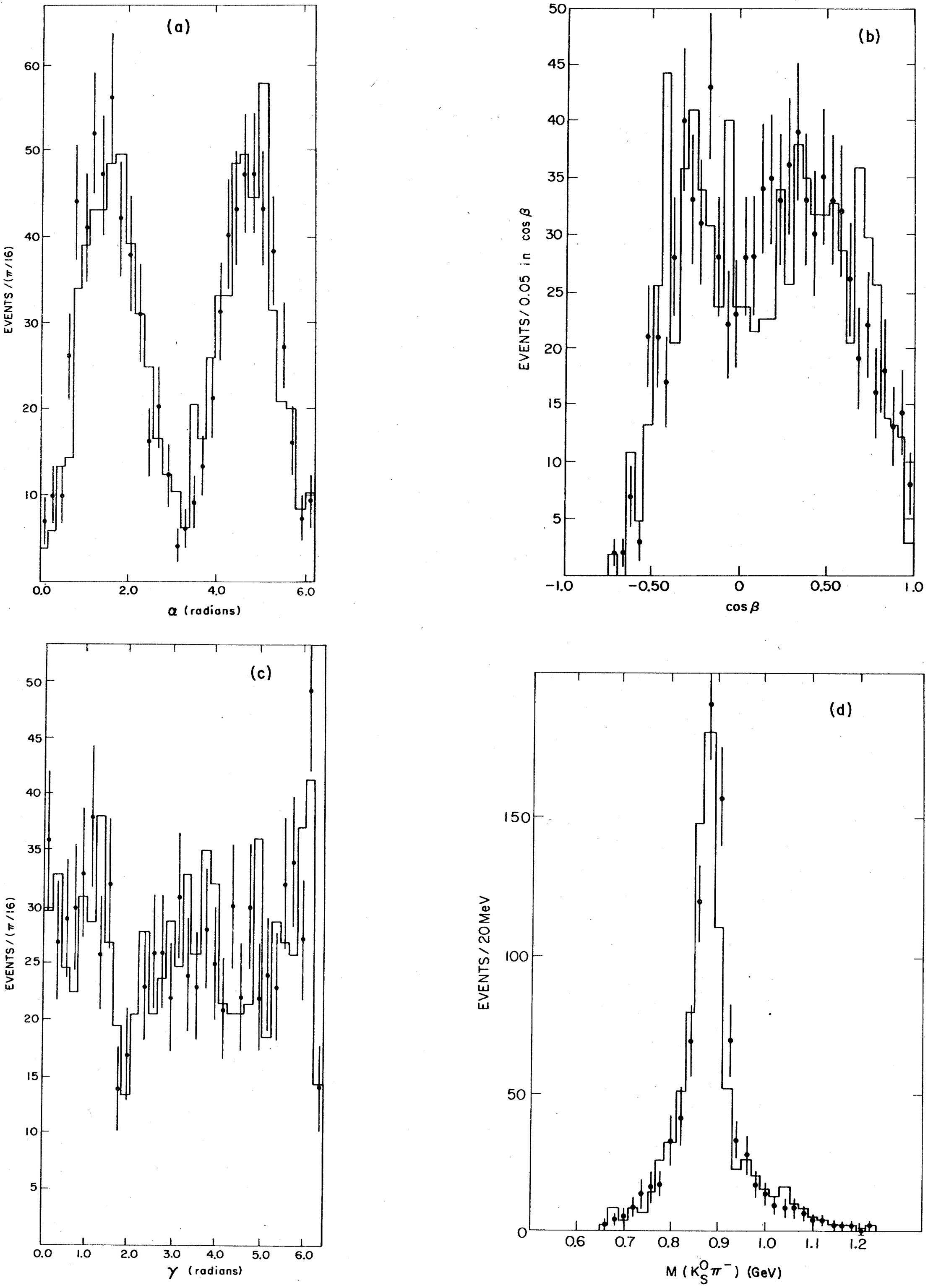

FIG. 10. Comparison of the 829 Monte Carlo–produced events (the histogram) according to our partial-wave solution with the 850 real data events (the points with error bars) at 1430 MeV. The histograms compare the three angle and two effective-mass plots described in the main text.

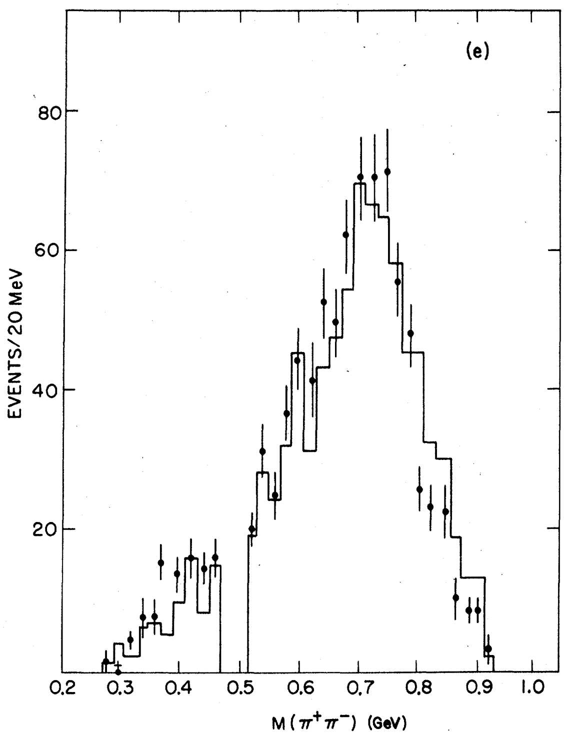

FIG. 10. *(Continued.)*

selected amplitudes. We made the same cuts as we did for the real data and then passed them through the Monte Carlo simulation of our apparatus. After this process we were left with 829 events to compare with 850 events in our real data sample. Figure 10 shows a comparison of this Monte Carlo data normalized to the real data for Euler angles α, β, and γ, and the $K\pi^-$ and $\pi^+\pi^-$ mass spectra. The absence of events at ~500 MeV in Fig. 10(e) is due to the K_S^0 cut (cut 8) on the $\pi\pi$ mass spectrum, as discussed in Sec. III. We have calculated the χ^2 for the five histograms using the statistical errors of the two event samples added in quadrature and obtained $\chi^2 = 153.5$ for 147 degrees of freedom. One can see that the agreement is quite good.

F. Estimation of N^* contamination

Our N^* cut (cut 10) eliminated many events with negative values of cosβ. This depletion is due to the strong correlation between $t_{K\pi}$ and cosβ, which makes the cosβ distribution a good place to examine N^* contamination in our data.

For the Monte Carlo events generated as described in Sec. IV E, we removed the N^* cut, normalized the $M(n\pi^+)$ distribution in the region $M(n\pi^+) > 1800$ MeV to the data with the N^* cut removed, and calculated the excess of the data over the Monte Carlo events in the region $M(n\pi^+) < 1800$ MeV. That excess is plotted as a function of cosβ in Fig. 11 (dashed histogram) along with the cosβ distribution of the data with the N^* cut removed (solid histogram). We see that before the cut the N^* contamination was small and confined to cosβ < 0.0.

G. The partial-wave solution from 1200 to 1600 MeV

In Fig. 12 the partial-wave amplitudes are plotted as a function of $K\pi\pi$ mass. (The figure has partial-wave amplitudes up to 2000 MeV. However, initially we consider only the amplitudes up to 1600 MeV; discussion of the region 1600–2000 MeV is deferred to a later section because of additional physics assumptions that were necessary in order to obtain these amplitudes.) The various curves on Fig. 12 represent the results of the mass-dependent fit described in Sec. V below.

Figure 12(a) shows the amplitude of the $0^-\kappa S0^+$ wave which is produced by natural-parity exchange. No strong variation with mass is noted in this wave: Presumably, it is a pure background wave. For the other natural-parity waves, we have used this wave as a reference for measuring the phase. In the 1200 to 1600 MeV region, we find only one other substantial natural-parity-exchange

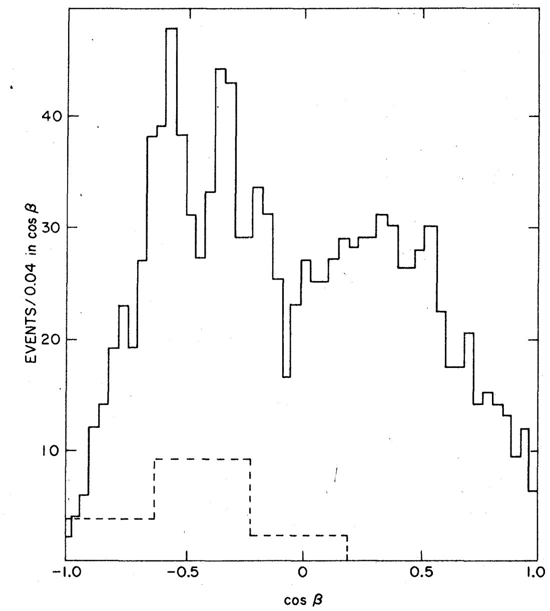

FIG. 11. cosβ distribution (solid lines) at 1430 MeV without the N^* cut described in the main text. The large binned histogram (dashed lines) in the lower left-hand corner represent the amount of N^*'s present in the data sample and its cosβ dependence.

wave, the $1^+K^*S0^+$ wave. There is a peak in the cross section for this wave at around 1400 MeV, together with a corresponding phase motion of 90° with respect to the 0^- wave as the mass varies from 1300 to 1500 MeV. This resonance is the $Q_2(1400)$.

Figure 12(d) shows the $1^-\rho P0^-$ wave which is produced by unnatural-parity exchange. This wave

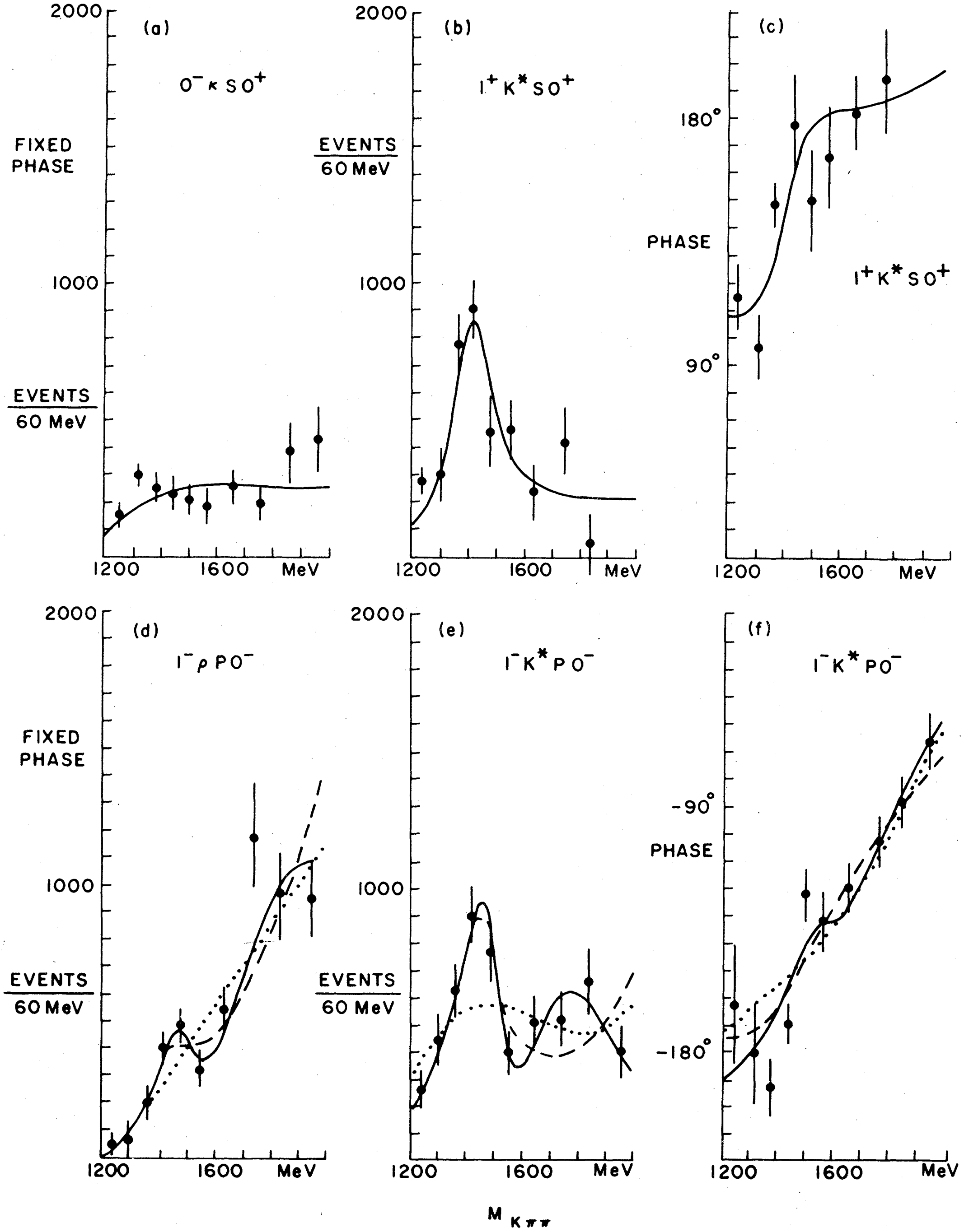

FIG. 12. The results of our partial-wave analysis for $K^-p\to K_S^0\pi^+\pi^-n$ for the $K^*\pi$, ρK, and $\kappa\pi$ amplitudes. The natural-exchange phases are measured relative to the $0^-\kappa S0^+$ wave, and the unnatural-exchange phases are measured relative to the $1^-\rho P0^-$ wave. See the text for a detailed description.

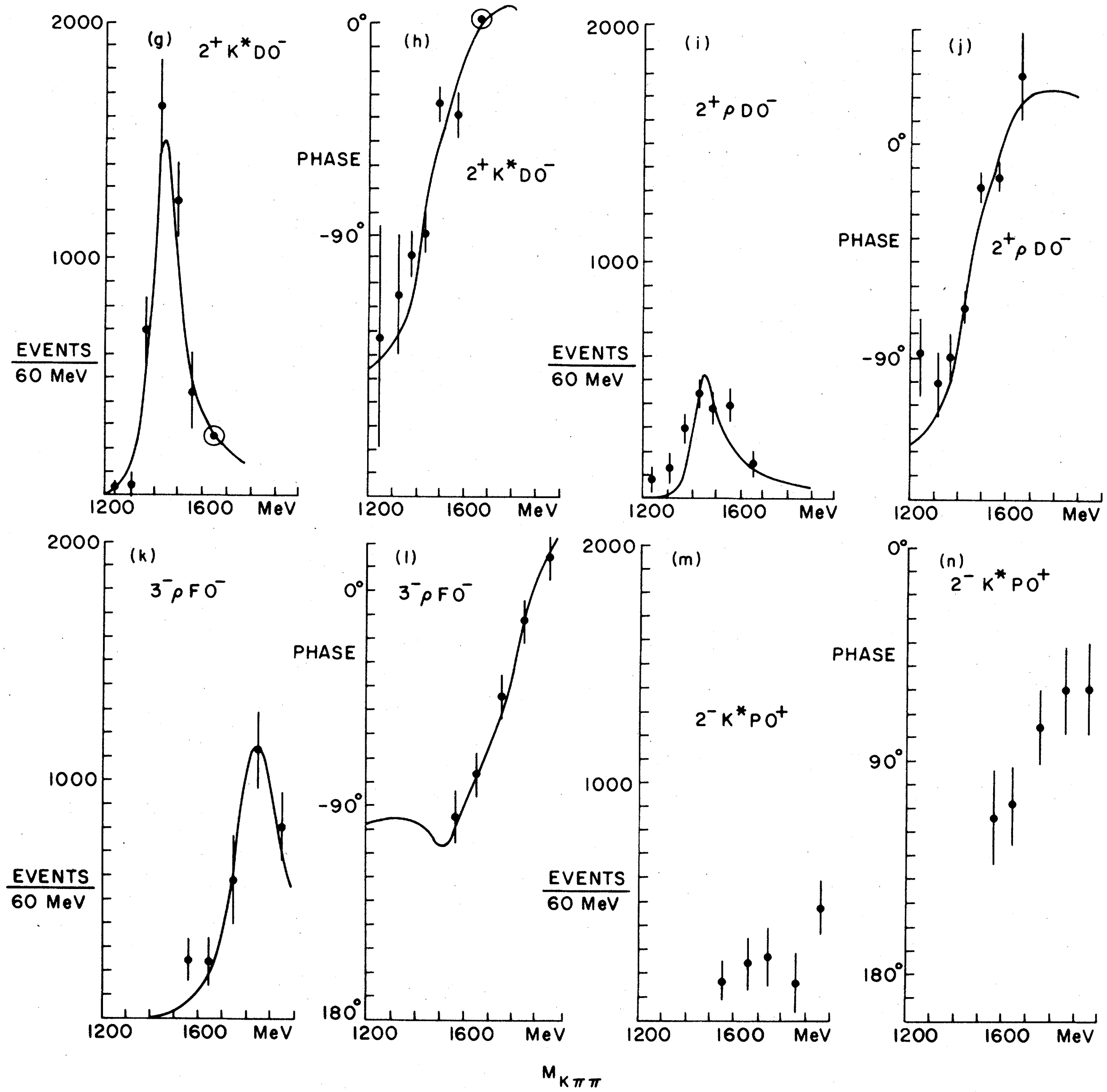

FIG. 12. *(Continued.)*

shows a relatively smooth rise as the mass increases, which is the behavior expected of a simple phase-space ρK production. We have used it as our reference wave for the unnatural-parity exchange waves. In the $2^+K^*D0^-$ wave we see a clear peak at 1430 MeV which corresponds to the well-known 2^+ resonance. We also see a clear phase motion with respect to our reference wave. The resonance also decays into the $2^+\rho D0^-$ wave. In this wave the peak is not as clear, but the phase motion is present. The other unnatural-parity state is the $1^-K^*P0^-$ wave. This wave shows a peak at ≈1450 MeV and has an associated phase motion of 80° across the peak. This is a candidate for a new resonance. This state will be discussed further in Sec. V B.

H. The propagation of the partial-wave solution to the 1600-2000 MeV region

Several difficulties were encountered in attempting to propagate our PWA solution to the mass region above 1600 MeV. From Table II and Fig. 7 we can see that the available data is decreasing rapidly as we move into the higher-mass region. In this region we used 100 MeV per bin. The dramatic falloff in the data is due chiefly to a falling acceptance of our apparatus. In addition, at higher masses we expect higher angular momenta will become important. Figure 13 shows the distribution in $\cos\beta$ expected from the important 3^- ($M = 0$) wave. An important feature distinguishing this wave from lower spins is the concentration near $\cos\beta = \pm 1$. However, the acceptance of the apparatus near $\cos\beta = \pm 1$ worsens as the mass increases, as is illustrated also in Fig. 13. The net outcome of falling statistics and acceptance is the loss of the ability to obtain a unique solution if one considers all possible 1^-, 2^+, and 3^- waves.

We made the following physics assumptions in order to obtain a continuous solution: First, that the 2^+ waves are produced only by the 1430 resonance, and thus must die out at higher energies. Second, that we expect to be able to observe only the ρK decay mode of the 3^- resonance at 1800 MeV. Beusch *et al.*[3] have done a similar analysis of $K^0_S\pi^+\pi^-$ at 10 GeV/c using the CERN Omega Spectrometer. They identified a dominant 3^- resonance at 1800 MeV which decayed 90% of the time into ρK. We constrained the contribution of the $2^+K^*D0^-$ wave to lie on the tail of the 1430 Breit-Wigner fit described in Sec. V. This is shown in Figs. 12(g) and 12(h) as the circled dot in the 1600-to-1700-MeV bin. Above 1700 MeV there is no contribution of this wave. We constrained the 3^- waves to consist of the single $3^-\rho F0^-$ contribution. With these two constraints the solution found at lower masses extrapolated smoothly to 2000 MeV. The only additional significant wave required was the $2^-K^*P0^+$.

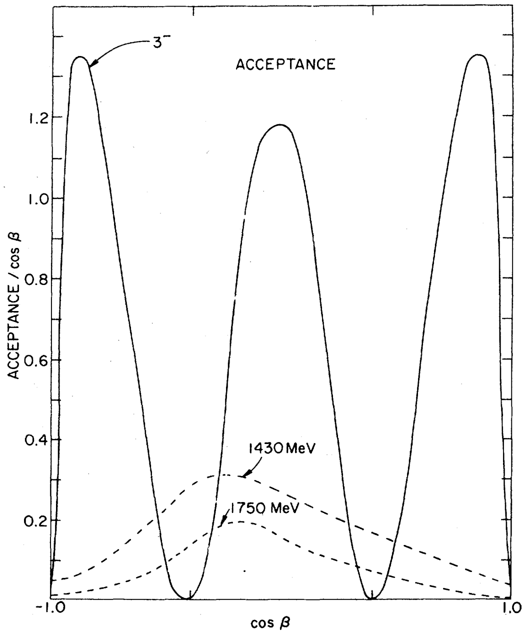

FIG. 13. The acceptance as a function $\cos\beta$ for phase space at 1430 and 1750 MeV. The 3^- $\cos\beta$ distribution is also shown.

The amplitudes are shown in Fig. 12. The $0^-\kappa S0^+$ wave and the $2^-K^*P0^+$ wave show no significant structure in this region. Let us consider the unnatural-parity-exchange states. We continue to use the $1^-\rho P0^-$ wave as our phase reference. In the higher-mass region it continues to grow in cross section. The $1^-K^*P0^-$ wave shows a possible small peak at 1850 MeV. This new peak is also associated with phase motion. We will discuss this wave further in Sec. V B.

As stated above, the $2^+K^*D0^-$ wave was constrained to follow a Breit-Wigner behavior. The $2^+\rho D0^-$ falls in cross section and has an appropriate phase change without any added constraints. As stated above, the only 3^- wave we have added is the $3^-\rho F0^-$ wave. This wave peaks at 1850 and has a resonancelike phase motion with respect to our reference wave.

J. Comparison with 4.2- and 10-GeV/c partial-wave analyses

In Fig. 14 we compare our partial-wave amplitudes with those obtained in a 4.2-GeV/c bubble-chamber experiment of Vergeest *et al.*[2] (hereinafter referred to as the 4.2-GeV/c analysis), and the 10-GeV/c CERN Omega Spectrometer experiment of Beusch *et al.*[3] (hereinafter referred to as the 10-GeV/c analysis). Since our experiment is at 6 GeV/c and the two other experiments are at 4.2 and 10 GeV/c, we need a method to normalize the data so that we can compare the results. Since neither of the other two analyses gives the complete isobar structure of the amplitudes, we will compare only the results of summing over the decay channels. Note also that the other analyses include a substantially larger region of t'. Since the 1430-MeV peak in the 2^+ wave is the most prominent (and best established) feature of all three analyses, this peak was chosen for normalization. The quoted Breit-Wigner curve from the 10-GeV/c analysis which is very close to the fitted curve of the 4.2-GeV/c analysis is shown as a dashed line in Fig. 14(a). We normalized our data so that the point at 1430 MeV lay on this curve. We see in Fig. 14(a) that there is good agreement among the three analyses for the 2^+ wave. This method of normalization will remove the effect of varying $t_{\min}$ in the region of 1430 MeV but is likely to be incorrect at higher masses.

Figure 14(a) shows the amplitude for the 1^- wave obtained in these experiments. Within the statistics the agreement is good apart from the two points at the highest masses in the 4.2 GeV/c

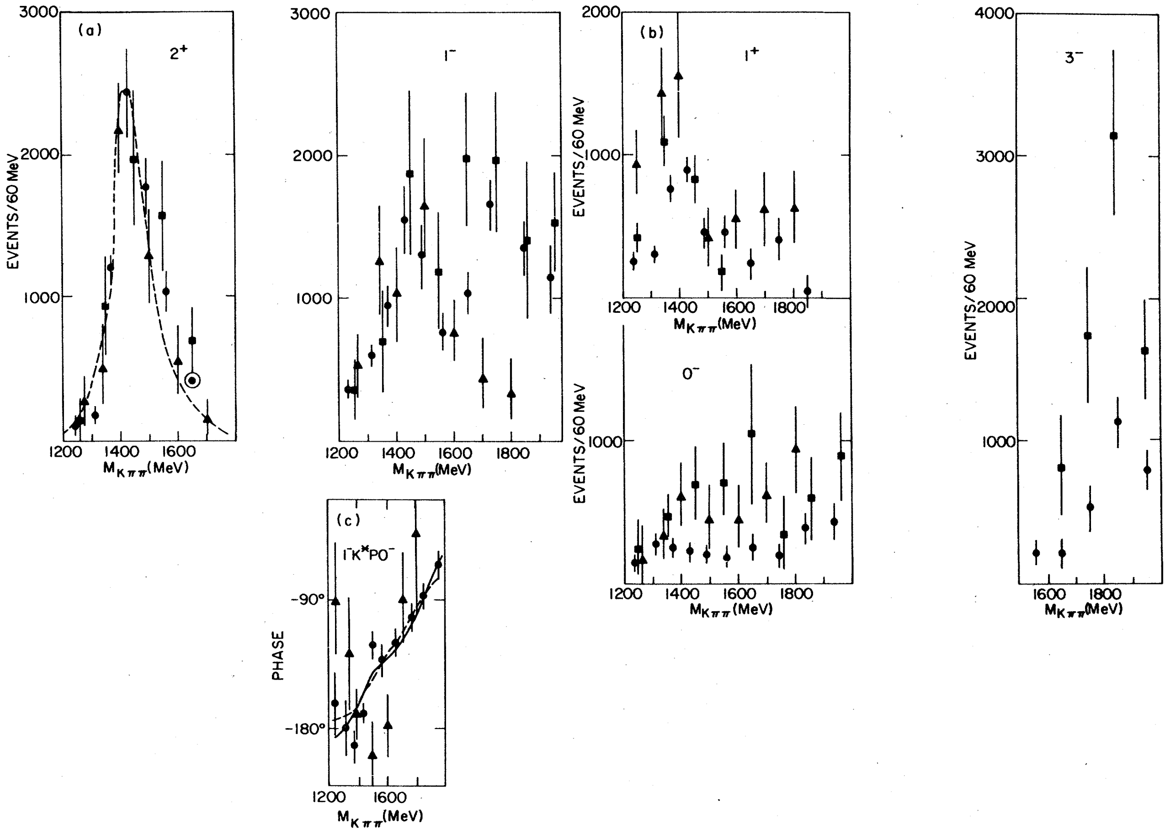

FIG. 14. A comparison of our partial-wave-analysis results (●) with those of the 4.2-GeV/c (▲) (Ref. 20) and 10-GeV/c (■) (Ref. 7) analyses. (a) 2^+ and 1^- amplitudes. (b) 1^+, 0^-, and 3^- amplitudes. (c) Comparison of the phase of the $1^-K^*P0^-$ wave relative to the $1^-\rho P0^-$ wave.

analysis which lie well below the other results. All the data in Fig. 14(a) are consistent with a bump in the 1^- wave at about 1450 MeV, although the larger errors in the 10-GeV/c data would lead to an inconclusive statement. The main difference in our data is in the phase of the 1^- wave. Figure 14(c) shows the phase of the $1^-K^*P0^-$ wave relative to the $1^-\rho P0^-$ wave for this experiment and the 4.2-GeV/c data. The 4.2-GeV/c analysis concluded that the 1^-K^* and $1^-\rho$ waves remained roughly 180° out of phase through the 1450-MeV region and that the 2^+K^* wave showed resonant phase motion relative to both 1^- waves. In our data, however, the 1^-K^* and 2^+K^* show very little relative phase motion [compare Figs. 12(f) and 12(h)] and both show substantial resonant phase motion with respect to the $1^-\rho$ wave, supporting the resonance interpretation of the bump in the 1^-K^* wave at 1450 MeV.

For the 1^+ wave all analyses give a breakdown according to decay channel, where the primary channel is via the K^* isobar. As may be seen in Fig. 14(b), the 1^+K^* wave shows the same general structure in all three analyses, although the detailed agreement is poor. Some of the disagreement may be due to the choice of 1^+ waves used to represent the data, in particular the inclusion of $M=1$ waves which were found to be insignificant in our analysis and the 10-GeV/c analysis. The disagreement in the 1^- phases may also be an artifact of the treatment of the 1^+ waves used in the 4.2-GeV/c analysis.

The 0^- (which is a pure background wave) of the other two analyses shows a higher level of background than our analysis. Finally, within the framework of this comparison the 3^- signal in the 10-GeV/c analysis is larger than ours, while the 4.2-GeV/c analysis found no evidence for any 3^- signal.

V. MASS-DEPENDENT FITS

We have fitted the amplitudes shown in Fig. 12 with a set of Breit-Wigner resonances and mass-dependent polynomial backgrounds. The fits were done by a least-square technique using the program MINUIT (Ref. 10) to minimize χ^2. Since the reference phase for the natural- and unnatural-exchange waves were different, we have done independent fits to these sets.

A. Natural-parity-exchange amplitudes

The reference wave is the 0^- state. We have parametrized this background wave as a second-order polynomial multiplied by a $\kappa\pi$ phase-space factor. Ordinarily the phase-space factor of a two-body system is related to its center-of-mass momentum. Since the κ is a very broad resonancelike structure in $K\pi$ scattering amplitude, its momentum or mass is not well defined. However, one can use the complex pole position of the κ as its mass and achieve a result very similar to what one would obtain from a more complicated method. The pole position used was $M_\kappa = (1250 - 500i)$ MeV, which approximates the 0^+ $K\pi$ phase shift. The center-of-mass momentum is then

$$q^2(\kappa,\pi) = \frac{[M_{K\pi\pi}{}^2 - (M_\kappa + M_\pi)^2][M_{K\pi\pi}{}^2 - (M_\kappa - M_\pi)^2]}{4M_{K\pi\pi}{}^2} .$$

Thus, the amplitude of the 0^- wave becomes

$$T(0^-) = \left[\frac{\mathrm{Re}[q(\kappa,\pi)]}{M_{K\pi\pi}}\right]^{1/2} [A + (B + iC)M_{K\pi\pi} + DM_{K\pi\pi}{}^2] ,$$

where the fit parameters A, B, C, and D are arbitrary real numbers. One should note that with this parametrization only a linear change in the phase was allowed. We restricted ourselves to this form since there was a danger of creating resonance structure if we had had the possibility of a quadratic variation of phase. We parametrized the 1^+ wave as a Breit-Wigner form multiplied by an arbitrary phase plus a constant background,

$$T(1^+) = \left[\frac{\mathrm{Re}[q(K^*,\pi)]}{M_{K\pi\pi}}\right]^{1/2} \left[\frac{Ae^{i\phi}}{M_0 - M_{K\pi\pi} - i\Gamma_T/2} + B + iC\right] ,$$

where

$$\Gamma_T = \frac{\mathrm{Re}[q(K^*,\pi)]}{M_{K\pi\pi}} \gamma^2 ,$$

and for the K^* pole we used

$$M_K^* = (890 - 25i) \text{ MeV}.$$

The fit parameters were M_0, the mass of the Q_2 resonance, and the arbitrary real numbers A, B, C, ϕ, and a coupling constant γ. The fit is plotted as the smooth curves in Figs. 12(a)–12(c). The parameters of the Breit-Wigner fit to the Q_2 are given in the first line of Table IV. Because of the absence of the Deck background, the bump in the $1^+K^*S0^+$ wave is one of the clearest indications of the Q_2 resonance to date. The mass and width are consistent with those derived from analyses of diffractive $K\pi\pi$ channels.[1]

The Q_1, which has been observed in the ρK channel in diffractive experiments, is not observed in our data. A similar situation has been observed in A_1 production where the 1^+ systems which are strongly coupled to the ρ are produced with small cross sections compared to other states and backgrounds in a charge-exchange reaction. In the reaction $\pi^-p \to A_1 n$ at 8 GeV/c the cross section is probably as low as $\frac{1}{2}$ μb compared to an A_2 cross section of 100 μb.[11] If a similar suppression occurs in this reaction, the Q_1 signal would be below our sensitivity.

B. Unnatural-parity-exchange amplitudes

For the $2^+K^*D0^-$ wave we used a pure Breit-Wigner form without a background. A Blatt-Weisskopf barrier factor was used with a radius of interaction, R, of around one Fermi:

$$T(2^+,K^*) = \frac{A(\{\mathrm{Re}[q(K^*,\pi)]/M_{K\pi\pi}\}F(K^*))^{1/2}}{M_0 - M_{K\pi\pi} - \frac{1}{2}i\Gamma_T} ,$$

where the barrier factor $F(K^*) = X^4/(X^4 + 3X^2 + 9)$ with $X = \mathrm{Re}[q(K^*,\pi)]R(2^+)$ and

$$\Gamma_T = \frac{\mathrm{Re}[q(K^*,\pi)]}{M_{K\pi\pi}} F(K^*)\gamma^2 .$$

The $2^+\rho D0^-$ wave was also described by the same Breit-Wigner form, but an extra phase rotation between the two 2^+ waves was added:

$$T(2^+,\rho) = \frac{B(\{\mathrm{Re}[q(\rho,K)]/M_{K\pi\pi}\}F(\rho))^{1/2}e^{i\phi}}{M_0 - M_{K\pi\pi} - \frac{1}{2}i\Gamma_T} .$$

The fitting parameters are the mass of 2^+K^* resonance M_0, and the real numbers A, B, ϕ, $R(2^+)$, and γ. For the 3^- and 1^- waves we used the analogous Breit-Wigner forms with a barrier factor for the appropriate angular momentum.

Finally, for the 1^- waves we found that we achieved the best description of the two channels if we included two resonances plus a phase-space background in both. However, we also did two other fits, one of which contained only one resonance plus a quadratic background and another which contained only a quadratic background. There is concern that with such a flexible background parametrization, one might simulate resonance behavior, including forward phase motion. However, this simulation should not be as efficient as a Breit-Wigner parametrization. Thus, if a resonance is truly present in the data it should take fewer parameters to obtain a reasonable fit.

The parameters for all of the Breit-Wigner resonances are given in Table IV and the fits appear as the curves in Fig. 12, where the solid line is the fit with two 1^- resonances, the dashed line is that with one 1^- resonance, and the dotted line is the fit with no 1^- resonances. The dashed and dotted lines only appear on the plots of the 1^- amplitudes because the change in other waves were minor. We see from the dotted line in the $1^- K^* \rho 0^-$ amplitude that the resonance-free background was trying to imitate resonancelike structure at 1490 MeV, especially the phase motion, but was unable to fit the data as well as a Breit-Wigner form. In fact, the χ^2 for the 1^- waves was 63 for 18 degrees of freedom for the fit with no resonances, compared to $\chi^2 = 45$ for 12 degrees of freedom for one resonance and $\chi^2 = 24$ for 14 degrees of freedom for two resonances. Thus, on the basis of χ^2 there is strong support for the existence of two 1^- resonances in our data. Given the specific physics assumptions necessary to obtain a fit in the high-mass region (see Sec. IVH), the evidence for the higher-mass 1^- resonance is not as strong as indicated by the χ^2 results.

The 2^+ fit parameters are consistent with the well-established properties of the $K^*(1430)$ in the $K\pi$ decay mode.[12] The radius parameter $R(2^+)$ was 4.47 GeV^{-1}, corresponding to $0.88f$. Since the fitted phase between the ρK and $K^*\pi$ decay modes was only 20°, the fit is consistent with the assumption of pure resonance production. This Breit-Wigner fit was used to fix the magnitude and phase of the $2^+ K^*$ wave above 1600 MeV. The mass of our 3^- fit is somewhat higher and the width somewhat larger than the world averages[12] but the range of the other measurements is large. Note that the effect of neglecting a rising background under the resonance in the 3^- wave would be to raise both the fitted mass and the width.

The errors listed in Table IV are standard deviations due to the statistical errors on the partial-wave amplitudes. Using a simulation of $E \times B$ effects in the Monte Carlo program we estimate the accuracy of our $K\pi\pi$ mass scale at 1420 MeV to be about 10 MeV, which is substantially smaller than the statistical errors on the Breit-Wigner peak locations. This estimate is consistent with the observed discrepancy of 0.7 MeV in the K_S^0 mass and 4 MeV in the $K^{*-}(890)$ mass.

TABLE IV. Results of least-squares fits to the partial-wave amplitudes for three hypotheses: no 1^- resonances, one 1^- resonance, and two 1^- resonances. The goodness of fit (χ^2) is given for the whole data sample and for the 1^- amplitudes and phases alone.

Fit	Two 1^- resonances			One 1^- resonance			No 1^- resonances		
χ^2/D.F. total	103/55			120/53			155/59		
χ^2/D.F. 1^- only	24/14			45/12			63/18		
J^P	Mass (MeV)	Width (MeV)	$\Gamma_{K^*\pi}/\Gamma_{K\rho}$	Mass (MeV)	Width (MeV)	$\Gamma_{K^*\pi}/\Gamma_{K\rho}$	Mass (MeV)	Width (MeV)	$\Gamma_{K^*\pi}/\Gamma_{K\rho}$
1^+	1415 ± 15	180 ± 10	large						
2^+	1450 ± 30	140 ± 30	~3	1450 ± 30	140 ± 30	~3	1450 ± 30	140 ± 30	~3
1^-	1500 ± 30	170 ± 30	~7	1450 ± 30	210 ± 30	~5			
1^-	1800 ± 70	500 ± 100	~12						
3^-	1850 ± 50	240 ± 50	small	1860 ± 50	280 ± 50	small	1860 ± 50	280 ± 50	small

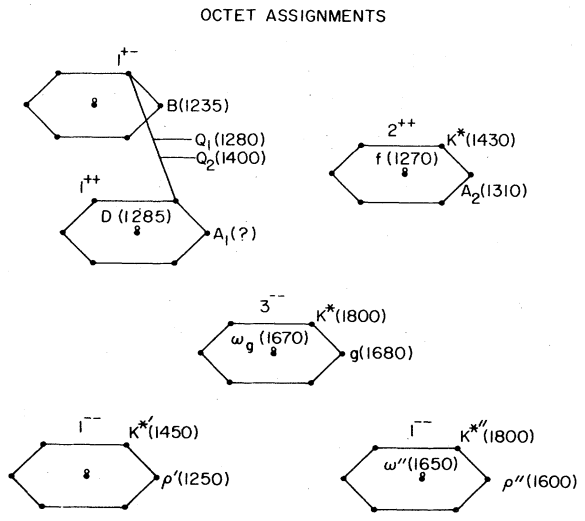

FIG. 15. Octet assignments of the observed resonance of this analysis.

VI. QUARK-MODEL ASSIGNMENTS

We attempt to relate the K^* states of Table IV to the simple quark model (see Fig. 15). The Q_2 meson is the 1^+ state which is that mixture of the P-wave $q\bar{q}$ states, Q_A ($J^{PC}=1^{++}$) and Q_B($J^{PC}=1^{+-}$), which decays predominantly into $K^*(890)\pi$. The $K^*(1430)$ ($J^{PC}=2^{++}$) is another P-wave $q\bar{q}$ state and is the strange member of the octet which includes the A_2 and the f.

Among possible D-wave $q\bar{q}$ states, the $K^*(1800)$ ($J^{PC}=3^{--}$) is a member of the g and ω_g octet. We see neither of the expected 2^- states and have two candidates for the expected 1^{--} state. However, the radial excitation of the S-wave $q\bar{q}$ system will lead also to a 1^- state (note that an analogous state

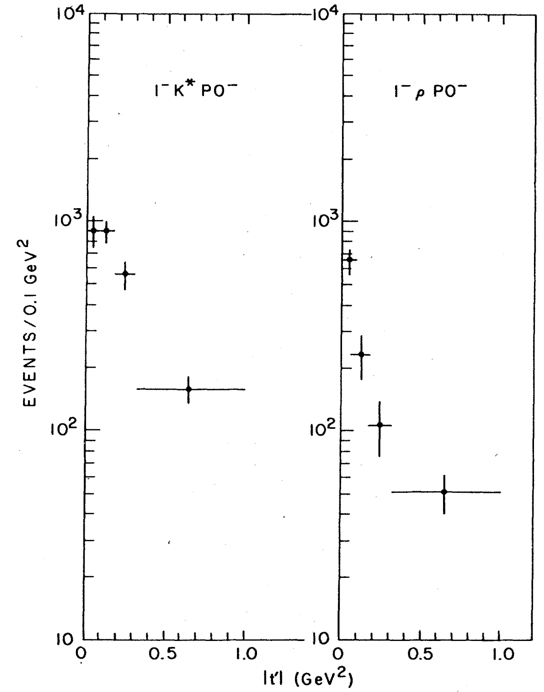

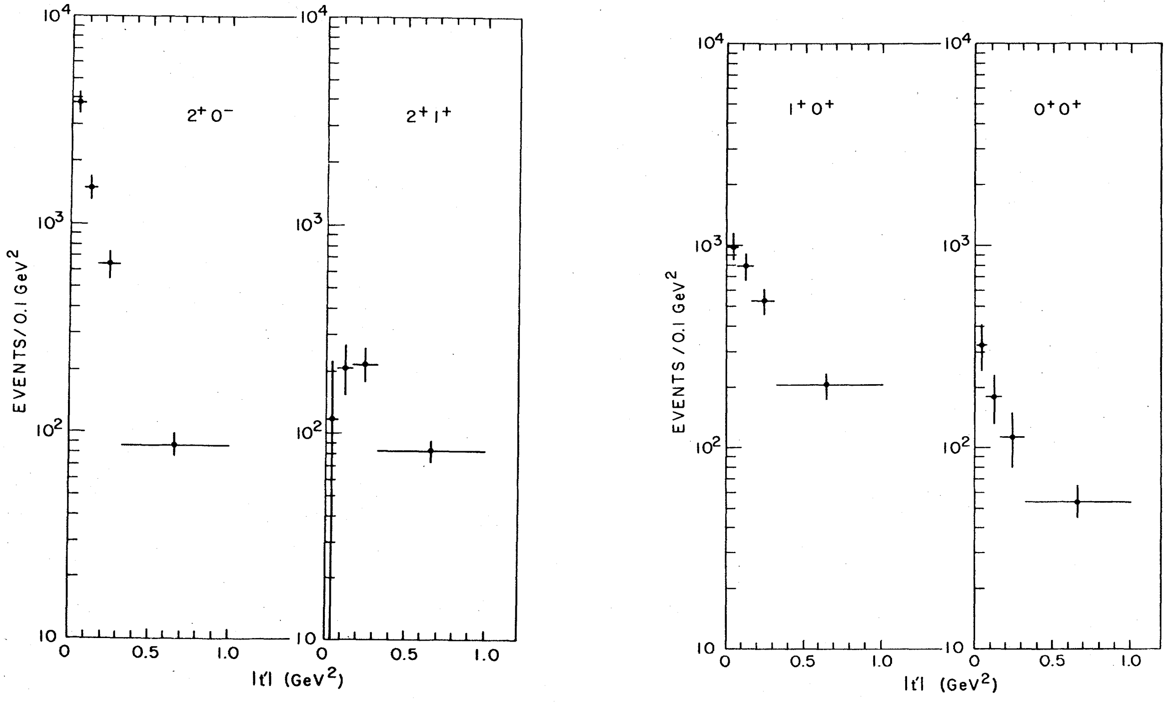

FIG. 16. The event distribution as a function of t' for each partial wave at 1430 MeV with a bin width of 120 MeV.

is seen in the charmonium spectrum). In Fig. 15 we have associated the 1500-MeV state with the ρ' (1250) and the 1800-MeV state with the ρ'(1600) and ω'(1650), since we would like to assign the lower octet to the radial excitation and the higher to the D-wave $q\bar{q}$ state in analogy with the charmonium situation. A difficulty with this assignment is the poor status of the ρ'(1250) and the nonobservation of the ω' associated with this octet. The ω' should decay into $\rho\pi$, but should be near the mass of the A_2. If it turns out there is such a state hidden by the A_2, it will greatly strengthen the case for two 1^{--} octets.

VII. t DEPENDENCE IN THE 1450-MeV REGION

We wish to examine the t dependence of production cross sections for various partial waves. Because of the limited statistics we concentrate on the region near 1450 MeV, which appears to contain three resonances. For this analysis, the mass range chosen was 1370 to 1490 MeV. The cut on $t_{K\pi\pi}$ (cut 9) described in Sec. III was removed while the N^* cut (cut 10) was retained.

The t dependence of the various partial waves is shown in Fig. 16. The data have been corrected for the acceptance of the apparatus. The cross section for the 2^+0^- wave shows an exponential fall with a slope of ≈ 7.5 GeV/c^{-2}, consistent with π exchange. On the other hand, the $1^-K^*P0^-$ wave has an exponential slope of ~ 3 GeV/c^{-2}, with a possible flattening at low $|t'|$, suggesting a mechanism other than pion exchange. The 1^+0^+ wave which contains the Q_2(1400) meson has an exponential slope of ~ 3 GeV/c^{-2}. Note that the fits to the latter two waves at small $|t|$ indicate significant nonresonant background, which might distort the shape of the differential cross section. The 2^+1^+ wave, which was found to be negligible for $|t'| < 0.2$ GeV/c^2, indeed shows a forward dip, but at a larger t the cross section is comparable to that of the $m = 0$ substate. Presumably this reaction proceeds via ρ exchange. The 0^-0^+ and $1^-\rho P0^-$ waves, which are dominated by nonresonant backgrounds, show sharp forward peaks with an exponential slope of ~ 7 GeV/c^{-2}.

We summed the contribution of the 2^+ wave to the four t' bins. The 120-MeV bin contains approximately half of the events in the integral of the Breit-Wigner shape (see Sec. V B) between threshold and 1750 MeV. The estimated detection efficiency, including nuclear attenuation of K^- in the target, decay of incident K^- in flight, K_S^0 branching ratio, trigger- and event-reconstruction inefficiencies and kinematic cuts, was 28%.[4] We calculate 30 ± 4 μb for the product of the cross section for the reaction $K^-p \to K^*(1430)n$, and the branching ratio for $K^*(1430) \to \bar{K}^0\pi^+\pi^-$. Figure 17 shows the comparison of our experiment with other measurements.[13]

VIII. SUMMARY

From a partial-wave analysis of the reaction $\pi^-p \to K_S^0\pi^+\pi^-n$ at 6 GeV/c we have observed resonant behavior in the 1^-, 1^+, 2^+, and 3^- waves and report masses and widths for these states in Table IV. We have measured the total production cross section and the t dependence of the $2^+K^*(1430)$ state at this energy. The Q_2 resonance $1^+K^*(1400)$ has been observed in diffractive processes, although the interpretation has been somewhat clouded by the presence of a large Deck background. In this experiment this resonance is seen clearly, with a relatively small background. We were able to clearly detect the $3^-K^*(1800)$ resonance through its major decay mode. We find a new 1^- resonance at around 1450 MeV, and have some evidence for another 1^- resonance at 1800 MeV. Finally, we discussed how these states might fit into the quark model.

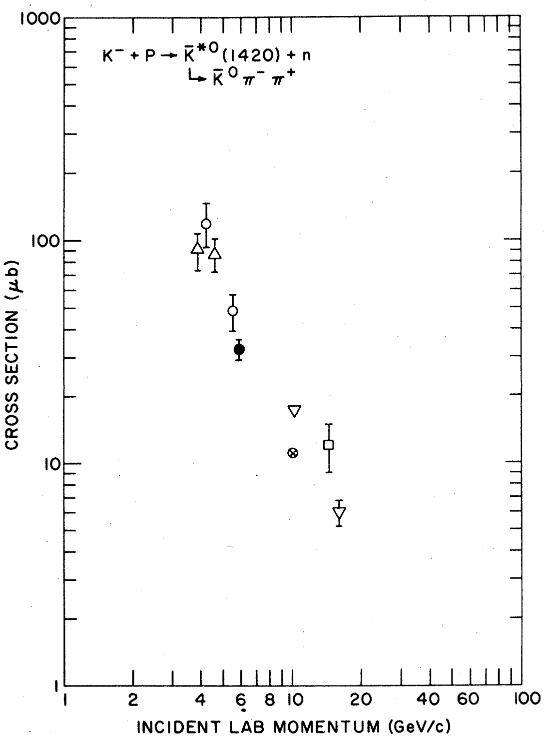

FIG. 17. Plot of the cross section at various incident K^- laboratory momenta for the reaction channel $K^-p \to K^*(1420)^0n$, where $\bar{K}^*(1420)^0 \to \bar{K}^0\pi^+\pi^-$. ⊗ Beusch *et al.*, Ref. 3. ○ Schweingruber *et al.*, Ref. 13. △ Aguilar-Benitez *et al.*, Ref. 13. □ Barloutaud *et al.*, Ref. 13. ▽ Otter *et al.*, Ref. 13. ● This experiment.

ACKNOWLEDGMENTS

We thank the members of the Alternating Gradient Synchrotron Division, the Particle Detector Division, and the Experimental Planning and Support Division of the Accelerator Department of BNL for their help in the execution of this experiment. We thank the technical support staff of the MPS and the OLDF for their aid. We acknowledge the help of A. Fainberg and S. Jacobs with the construction of some of the apparatus, S. Eiseman during the data taking, and I-J. Kim during the early analysis phase of this measurement. This research was supported by the U. S. Department of Energy under Contract No. DE-AC02-76CH00016. The City College of New York work was supported by the National Science Foundation and the City University of New York PSC-BHE Research Award Program.

---

*Present address: Florida State University, Tallahassee, Florida 32306.

[1] Yu. M. Antipov *et al.*, Nucl. Phys. B86, 381 (1975); M. Spiro *et al.*, Phys. Lett. 60B, 389 (1976); G. W. Brandenburg *et al.*, Phys. Rev. Lett. 36, 703 (1976); 36, 706 (1976); 36, 1239 (1976); G. Otter *et al.*, Nucl. Phys. B106, 77 (1976); R. K. Carnegie *et al.*, Phys. Lett. 63B, 235 (1976); R. Baldi *et al.*, *ibid.* 63B, 344 (1976); K. Hendrick *et al.*, Nucl. Phys. B112, 189 (1976); S. U. Chung *et al.*, Phys. Rev. Lett. 40, 355 (1978); Ph. Gavillet *et al.*, Phys. Lett. 76B, 517 (1978), P. Estabrooks *et al.*, Nucl. Phys. B133, 490 (1978); G. Otter *et al.*, *ibid.* B147, 1 (1979); J. S. M. Vergeest *et al.*, *ibid.* B158, 265 (1979).

[2] J. S. M. Vergeest *et al.*, Phys. Lett. 62B, 471 (1976).

[3] W. Beusch *et al.*, Phys. Lett. 74B, 282 (1978).

[4] U. Mallik, City College of New York, Ph.D. thesis, 1978 (unpublished).

[5] F. T. Solmitz, A. D. Johnson, and T. B. Day, Alvarez Group Programming Note P117, LRL (unpublished).

[6] A. Etkin *et al.*, Phys. Rev. Lett. 36, 1482 (1976).

[7] D. J. Herndon, P. Söding, and R. J. Cashmore, Phys. Rev. D 11, 3165 (1975).

[8] P. Eberhard, Comput. Phys. Commun. 3, 296 (1972); 5, 163 (1973).

[9] D. J. Herndon *et al.*, Phys. Rev. D 11, 3183 (1975).

[10] F. James and M. Roos, Comput. Phys. Commun. 10, 343 (1975).

[11] A. C. Irving and H. R. Sepangi, Nucl. Phys. B139, 327 (1978).

[12] Particle Data Group, Phys. Lett. 75B, (1978).

[13] F. Schweingruber *et al.*, Phys. Rev. 166, 1317 (1968); M. Aguilar-Benitez *et al.*, Phys. Rev. D 4, 2583 (1971); R. Barloutaud *et al.*, Nucl. Phys. B59, 374 (1973); G. Otter *et al.*, *ibid.* B84, 331 (1975).